Vertical Surface Phononic Mach-Zehnder Interferometer

Rahman Sharaf[1] Sara Darbari,[1,*,†] and Abdelkrim Khelif[2]

[1]*Nano Sensors and Detectors Laboratory, Nano Plasmophotonic Research Group, Faculty of Electrical and Computer Engineering, Tarbiat Modares University, Tehran 1411713116, Iran*

[2]*FEMTO-ST Institute, CNRS UMR-6174, Université de Bourgogne Franche-Comté, 25000 Besançon, France*

In this work, we propose and explore a double-stage phononic crystal (PnC) consisting of a top suspended ZnO layer, an array of sandwiched Si pillars, and a bottom ZnO layer on a Si substrate. The proposed double-stage PnC exhibits interesting behavior of routing the incident surface acoustic waves (SAWs) based on polarization and frequency, so that it can be considered as an efficient building block for alternative multistage SAW components. Here, we design the double-stage PnC to behave as an efficient vertical SAW splitter in a Mach-Zehnder interferometer, using the excitation of appropriate surface-coupled modes through the periodic locally resonating pillars. Benefiting from the acoustoelectric effect in ZnO, the exposed top ZnO layer serves as the sensing branch, and the bottom ZnO layer serves as the reference branch in the presented vertical Mach-Zehnder interferometer. The vertical configuration of the proposed design allows exposure of the top ZnO layer to external stimulations, such as exposure to ultraviolet illumination or a hydrogen environment, while protecting the underlying parts from being exposed. This structural aspect simplifies the experimental implementation of our design in comparison with the conventional planar Mach-Zehnder interferometers by avoiding the necessity of in-plane focusing of external stimulation on the sensing branch. Our optimized Mach-Zehnder interferometer shows an output transmission signal of -8 dB and a high extinction ratio of 23 dB at 8.6 GHz when the conductivity of the top ZnO layer is increased from about 1 S/m to 100 S/m via external stimulation. Here, we propose a highly sensitive miniature vertical surface acoustic Mach-Zehnder interferometer, which may open up alternative horizons for future multistage SAW components.

I. INTRODUCTION

Surface acoustic wave (SAW) devices with miniature micrometer-scale dimensions were first introduced in 1965 to replace bulky electromagnetic elements (millimeter to meter scale) in radar applications, taking advantage of slow elastic phonons instead of high-speed photons [1]. Since then, SAW devices have attracted the interest of researchers in various application fields, including different sensor types [2–4], on-chip rf filters [5], microfluidics [6], quantum technology [7], acoustoelectric and acousto-optic components [8–10], and nonreciprocal SAW components [11–13]. On the other hand, phononic crystals (PnCs) allow the control of propagation characteristics of acoustic and elastic waves in applications such as filters [14], demultiplexers [9,15,16], sensors [17,18], thermal transport engineering [19,20], energy harvesting [20,21], and resonators [22]. PnCs for controlling SAWs can be realized by placing holes or pillars on the surface of a substrate. However, pillars have the advantage of behaving as local resonators at specific acoustic frequencies, opening low-frequency local surface resonance gaps [23,24], in addition to conventional Bragg gaps at higher frequencies.

It is known that elastic wave propagation in piezoelectric semiconducting materials, such as ZnO, gives rise to a traveling electric field [25] and the acoustoelectric (AE) effect, which modulates both the velocity and attenuation of elastic wave propagation. It has been proved that taking advantage of the AE effect in piezoelectric semiconducting materials, embedded as delay lines in SAW devices, allows modulation of the output device behavior by controlling the electrical conductance (σ) through external stimulation [26]. The AE effect has been exploited to realize sensitive SAW devices in applications such as hydrogen [27], ultraviolet (UV) light [28], and biological [29] sensors, as well as tunable elastic waveguides and demultiplexers [9,14].

In this research, we propose a highly sensitive vertical surface acoustic Mach-Zehnder interferometer, suitable for detecting external stimulation such as UV illumination or exposure to environmental gases such as hydrogen. Our proposed vertical Mach-Zehnder device consists of a Si-pillar-based PnC as the elastic wave splitter, which is sandwiched between two ZnO layers. The top ZnO layer

*sara.darbari@gmail.com
†s.darbari@modares.ac.ir

serves as the suspended sensing branch, exposed to external stimulation, while the bottom ZnO layer serves as the reference branch. The presented double-stage PnC enables the potential for efficient splitting or routing of the incident SAWs, which may lead to alternative SAW devices for different applications, such as sensors or acousto-optic components. Our presented CMOS-compatible, highly sensitive vertical surface acoustic Mach-Zehnder design in the gigahertz frequency range benefits from a high extinction ratio, acceptable transmission signal, and simple implementation without the need for exerting local external stimulation, and can open an alternative horizon in efficient real-time detection applications.

II. THEORY AND IMPLEMENTATION OF SIMULATION

It is well known that surface local resonators on a substrate can be coupled to SAWs at certain resonance frequencies. Accordingly, PnCs consisting of an array of local resonators, such as pillars, can lead to low-frequency surface-coupled guiding modes with dispersion behavior depending on the elastic coupling between the resonators. The weaker elastic coupling leads to the less dispersive surface-coupled bands, and a probable local resonance band gap is opened at low frequencies. Conversely, stronger elastic coupling between the individual resonators results in highly dispersive bands, and the closing of the local resonance band gaps. Elastic coupling can generally be tuned by the interspacing distance between the resonators, which is the basic principle of designing coupled-resonator surface acoustic waveguides with tunable guiding mode dispersion and pass band FWHM [14]. Here, we introduce a suspended top layer on the pillar array to add a second degree of freedom to tune the elastic coupling between the resonators with a fixed interspacing distance. Thus, we expect stronger elastic coupling and more dispersive surface-coupled modes when increasing the thickness of the top layer. This double-stage PnC-based configuration can allow the emergence of a higher number of surface-coupled modes with different contributions from the bottom and top surfaces. In other words, we can achieve different low-frequency surface-coupled modes in which the elastic wave is dominantly propagating on the bottom or top surface, or both simultaneously. This behavior can be applied as a vertical SAW splitting behavior in which pillars couple the elastic wave to the bottom or top surface with a frequency-dependent coupling strength. Here, we elaborate the full behavior of the proposed double-stage PnC as the vertical splitter in our SAW Mach-Zehnder design. In this case, splitting portions are equal, so that the top and bottom surfaces act as the two waveguides for SAW propagation. In such a Mach-Zehnder design, the bottom surface is protected from the external stimulation, such as light illumination or gas absorption, by

the top layer. Hence, the output behavior can be strongly affected by slight variations in the elastic properties of the top layer in response to external stimulation. Here, we propose the AE effect of piezoelectric layers, such as ZnO, as the transduction mechanism in the top branch. Hence, the ZnO conductivity (σ) is assumed to be modulated in the top layer when exposed to external UV illumination or gases like hydrogen [25]. To calculate the band structure of the proposed double-stage PnC we assume a unit cell with lattice constant a consisting of cylindrical Si pillars, with radius r and height h_p, connecting the top and bottom ZnO thin films [Fig. 1(a)]. Moreover, the thicknesses of the top and bottom ZnO thin films are h_u and h_d, and the substrate is made up of Si with thickness h_s. Periodic boundary conditions (PBCs) are assumed along the $\pm x$ and $\pm y$ directions, as shown in Fig. 1(a), while the boundary condition at the bottom of the substrate ($-z$ direction) is assumed to be fixed. To investigate the SAW transmission behavior of the proposed double-stage PnC structure, a supercell with 11 rows of pillars along the SAW propagation ($+x$ direction) is considered, as shown in Fig. 1(b). Sidewalls of the supercell along the $\pm y$ directions are assumed to be PBCs, while sidewalls along $\pm x$ and $-z$ axes are assumed to be perfectly matched layers (PMLs) to effectively suppress the boundary reflections. Here, we consider a SAW line source on the surface of the bottom ZnO thin film, which is labeled In in Fig. 1(b). Moreover, we consider the double-stage PnC in Fig. 1(b) as a three-output terminal component, and define three different output cut lines as FD, FU, and RU to calculate the corresponding transmissions. To achieve the transmission (T), we calculate the integral of the elastic potential energy along the output cut lines by Eq. (1), normalized to the input elastic potential energy.

$$\text{Elastic Potential Energy} = u_x^2 + u_y^2 + u_z^2, \quad (1)$$

where $u_{x,y,x}$ are the displacement components.

To evaluate the shear horizontal (sagittal) transmission, we consider the shear (sagittal) polarized source with
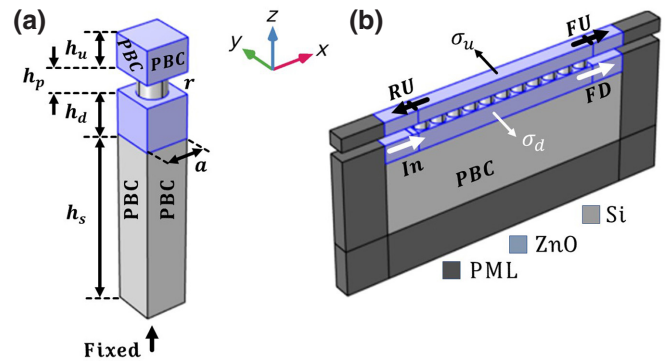

FIG. 1. (a) Unit cell of the PnC used for calculating the band structure. (b) Supercell of the finite PnC with 11 rows of pillars along the wave propagation direction ($+x$) used for calculating the transmission spectrum.

TABLE I. Parameters of the unit cell and supercell structures shown in Fig. 1.

Parameter	Symbol	Value (nm)
Pillar radius	r	85
Pillar height	h_p	100
Lattice constant	a	200
Top ZnO layer	h_u	150
Bottom ZnO layer	h_d	200
Si substrate thickness	h_s	800

displacement component(s) in the y (x, z) direction(s).

The PBC obeys the Bloch-Floquet theorem for elastic waves as follows [30]:

$$u_i(x + a, y + a) = u_i(x, y)e^{-i(k_x a + k_y a)}, \tag{2}$$

where k_x and k_y are the Bloch wave vectors.

The values of all the structural parameters are summarized in Table I. The lattice constant of the PnC is set at 200 nm to achieve the surface-coupled splitting behavior in the gigahertz frequency range. We have presented a comprehensive investigation of the structural parameters of a single-stage PnC (r, h_p) in our previous work, which leads us to choose similar dimensions here (Table I) to achieve reasonable transmission values [11]. Moreover, it should be noted that the thicknesses of both top and bottom ZnO layers (h_u, h_d) are found through optimization of the behavior of the final proposed SAW Mach-Zehnder device, which is discussed in the next section. However, considering that the surface elastic waves penetrate about one wavelength into the substrate, we assume $h_s + h_d = 5a$ to avoid the SAW confinement effects in the substrate along the z direction.

It is well established that for linear nonpiezoelectric materials, such as Si, two coupled equations, Eqs. (3) and (4), govern the elastic wave propagation [14],

$$S_{ij} = \frac{1}{2}(\partial_j u_i + \partial_i u_j), \tag{3}$$

$$T_{ij} = C_{ij} S_{ij}, \tag{4}$$

where S_{ij}, T_{ij}, and C_{ij} show the strain, stress, and the elastic stiffness components along $i,j = x,y,z$ directions. Si is

a symmetric crystalline semiconductor material, and has three independent anisotropic elastic constants including $C_{11} = 165.7$, $C_{12} = 63.9$, and $C_{44} = 79.9$ GPa, and the mass density of $\rho = 2331$ kg/m^3 [30].

On the other hand, in piezoelectric semiconductors, such as ZnO, propagation of the elastic waves coincides with a strain-induced electric field. Hence, elastic wave propagation in ZnO can be described by the coupled equations (5) and (6) [31],

$$T = CS - e^T E, \tag{5}$$

$$D = eS - \varepsilon E, \tag{6}$$

wherein e, ε, D, and E are the piezoelectric coupling and dielectric matrices, and the electric displacement and electric field, respectively.

According to AE effect in piezoelectric semiconductor materials like ZnO, variation of carrier concentration and the consequent conductivity variation affect the elastic wave propagation. This effect is attributed to the screened electric field associated with the elastic wave propagation by the free carriers. The acoustoelectric effect leads to a modulation of elastic wave velocity and attenuation by the carrier concentration or the correlated conductivity value. Assuming plane wave propagation for D and E in a conductive volume, Eq. (7) describes the relation between the current density (J) and the electric displacement and electric field [14],

$$D = -\frac{j}{\omega}J = -\frac{j}{\omega}\sigma E, \tag{7}$$

wherein σ is the conductivity of the piezoelectric semiconductor and ω is the angular frequency and $j = \sqrt{(-1)}$.

Defining an effective AE elastic matrix (C') for the piezoelectric semiconductor, Eqs. (5)–(7) can be combined to describe the coupling effect between strain and stress as [31]

$$T = C'S. \tag{8}$$

For ZnO, as an anisotropic crystal, elastic matrix elements are $C_{11} = C_{22} = 209.71$, $C_{12} = 121.14$, $C_{13} = C_{23} = 105.39$, $C_{33} = 211.19$, $C_{44} = C_{55} = 42.37$, and $C_{66} = 44.24$ GPa, and the mass density is $\rho = 5680$ kg/m^3. Accordingly, the effective AE matrix is established as [14]

$$[C'] = \begin{bmatrix} C_{11} + e_{31}^2 Y_{33} & C_{12} + e_{31}^2 Y_{33} & C_{13} + e_{31}^2 Y_{33} & 0 & 0 & 0 \\ C_{12} + e_{31}^2 Y_{33} & C_{11} + e_{31}^2 Y_{33} & C_{23} + e_{31}e_{33}Y_{33} & 0 & 0 & 0 \\ C_{13} + e_{31}e_{33}Y_{33} & C_{23} + e_{31}e_{33}Y_{33} & C_{33} + e_{33}^2 Y_{33} & 0 & 0 & 0 \\ 0 & 0 & 0 & C_{44}e_{15}^2 Y_{22} & 0 & 0 \\ 0 & 0 & 0 & 0 & C_{44} + e_{15}^2 Y_{11} & 0 \\ 0 & 0 & 0 & 0 & 0 & C_{66} \end{bmatrix}, \tag{9}$$

wherein Y is a 3×3 matrix with elements defined by Eq. (10),

$$Y = \begin{bmatrix} \frac{1}{(j/\omega)\sigma + \varepsilon_{11}} & 0 & 0 \\ 0 & \frac{1}{(j/\omega)\sigma + \varepsilon_{22}} & 0 \\ 0 & 0 & \frac{1}{(j/\omega)\sigma + \varepsilon_{33}} \end{bmatrix}. \quad (10)$$

All simulations to achieve the band structures and transmissions are carried out using the finite-element method.

III. OPERATIONAL PRINCIPLE OF THE DOUBLE-STAGE PHONONIC CRYSTAL

Figures 2(a)–2(c) show the calculated band structures for the first 35 bands of the unit cells shown in Figs. 2(g)–2(i), which correspond to the bare Si substrate,

ZnO-coated Si substrate, and the single-stage PnC consisting of a Si pillar array on the ZnO/Si substrate, respectively. The inset of Fig. 2(a) shows the irreducible path in the first Brillouin zone of the investigated PnCs with a square lattice. Figures 2(d)–2(f) display the band structures for the double-stage PnC with the top ZnO layer thickness (h_u) of 50, 100, and 150 nm, respectively. It is notable here that the conductivity of top and bottom ZnO layers are assumed to be zero ($\sigma_u = \sigma_d = 0$) as the extreme limit of the intrinsic conductivity in such a wide-gap semiconductor. This intrinsic condition corresponds to an absence of any external stimulation that can modulate the conductivity of the top ZnO layer, such as exposure to UV illumination or a hydrogen environment. Moreover, all the bands are depicted in colors showing their sagittal-to-shear polarization ratio. To achieve this ratio at each point of the
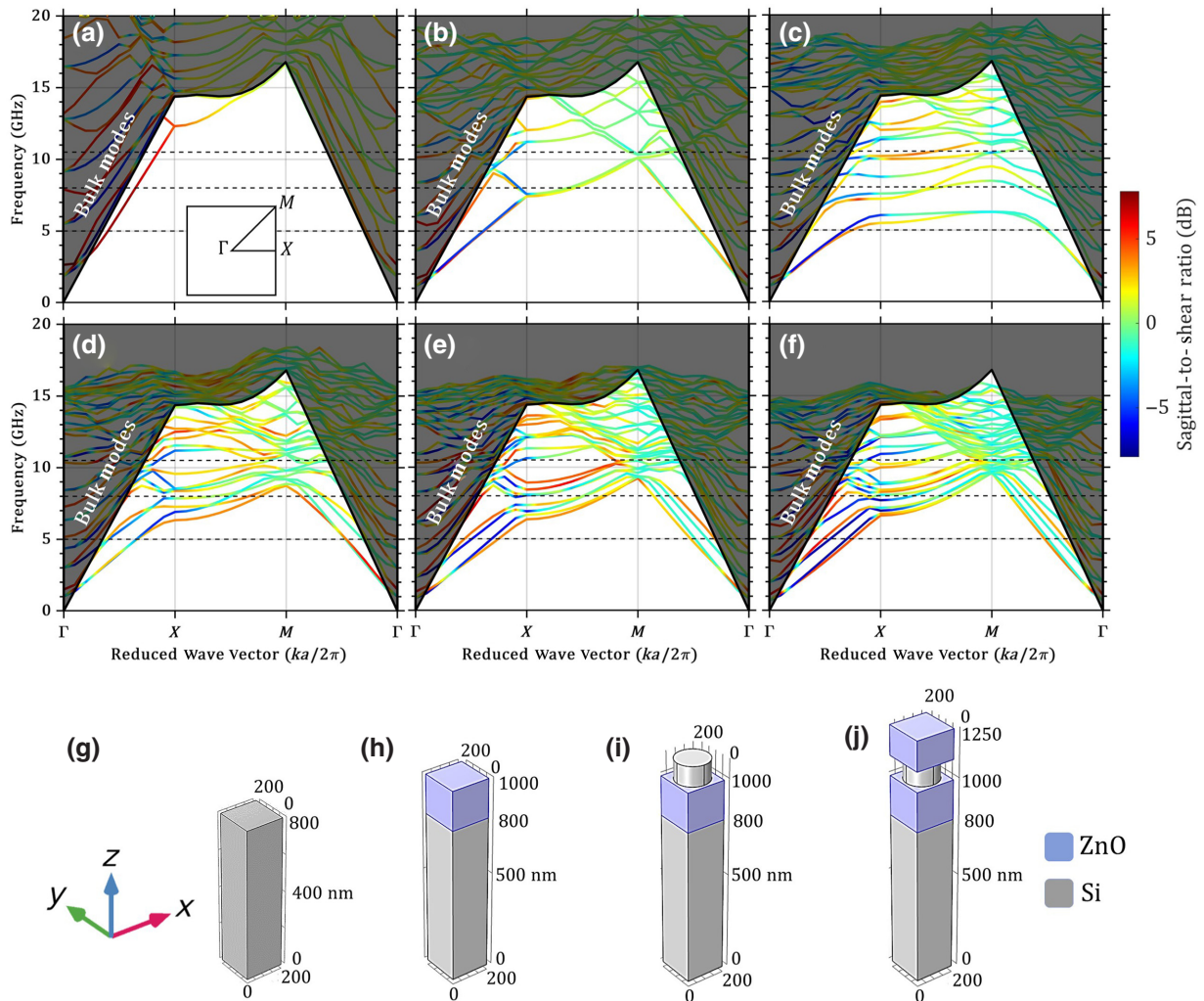

FIG. 2. (a)–(c) Band structures of the unit cell shown in (g)–(i), respectively. Inset in (a) shows the irreducible first Brillouin zone of the square lattices. (d)–(f) Band structures of the unit cell shown in (j) with different thicknesses of the top ZnO layer, corresponding to $h_u = 50$, 100, and 150 nm, respectively. (g) Unit cell corresponding to bare Si substrate. (h) Unit cell consisting of a ZnO thin film on the bare Si substrate. (i) Unit cell consisting of a Si pillar on ZnO/Si substrate. (j) Unit cell of the double-stage PnC, consisting of Si pillars sandwiched between a top suspended ZnO layer and a bottom ZnO layer on Si substrate.

bands, we calculate the maxima between the integral of sagittal displacement components (*x*-*z* plane) to the integral of the shear displacement component in the unit cell. The dark gray area in the band structures covers the bulk modes with higher velocities, and the rest indicates the surface elastic modes with lower group velocities. The interface between the bulk and surface modes is defined by the sonic cone, corresponding to the bulk modes with the lowest velocities.

We show the constant frequencies of 5, 8, and 10.5 GHz by horizontal dashed lines in all the band structures. As it is shown in Fig. 2(a), the Si substrate only supports two pure sagittal surface bands in the Γ-X direction, as we presented in our previous report [11]. Adding a ZnO thin film on top of the Si substrate [Fig. 2(h)] leads to the emergence of more surface modes with both sagittal and shear polarizations, as shown in Fig. 2(b). It can be observed that the first and second surface bands are purely sagittal and purely shear polarized in the Γ-X direction, respectively. Moreover, the ZnO/Si substrate leads to a negative slope or negative group velocity along the Γ-X direction in some surface bands, such as the third and fourth ones in Fig. 2(b). These negative group velocities force the phases of elastic waves to propagate in opposite directions, and can be used to design lenslike behavior to focus the elastic waves in specific directions [32]. It can be observed in Fig. 2(c) that by adding pillars on top of the bottom ZnO layer, the negative group velocity of the surface bands vanishes and the low-frequency surface-coupled bands are nearly isolated, as compared with Fig. 2(b). In this PnC, surface-coupled modes are constructed between resonating modes of pillars and the surface modes of the substrate. The localized resonating behavior of the emerging surface-coupled modes leads to lower dispersive modes and flatter bands, and leads to the observed partial isolation of the lower bands in Fig. 2(c). Finally, by adding the top ZnO layer on the pillars in Fig. 2(j), the negative slope reappears in some of the intermediate surface bands [Figs. 2(d)–2(f)]. For instance, the negative slope emerges in the fifth to eighth bands along the Γ-X direction in Fig. 2(e). It is shown in Figs. 2(d)–2(f) that increasing h_u leads to low-frequency surface-coupled bands with higher dispersive behavior, which can be attributed to stronger elastic coupling between the local resonating pillars through the top ZnO layer. Moreover, the polarization purity of the low-frequency surface-coupled bands increases for thicker top ZnO layers, which is again related to the stronger coupling between the resonating pillars that can break the degeneracy in the bands, splitting them into individual highly dispersive single-mode surface-coupled bands, which are dominantly sagittal or shear. The other observation is the emergence of a higher number of surface modes for thicker top ZnO layers, which is related to the emergence of new elastic modes across the top ZnO layer that can take part in new coupled elastic modes in the whole structure.

Another phenomenon that should be noted is the polarization exchange between two modes that approach each other. For example, the first two bands in Fig. 2(e) have shear and sagittal polarizations at the Γ point, while, after approaching at around 2 GHz, they exchange their polarizations.

To evaluate the effect of conductivity variations on the eigenmodes of the investigated double-stage PnC, we consider the upper and lower extreme limits of the conductivity value exclusively, in which the frequency-dependent term in Eq. (8) vanishes and allows calculation of the related band structures. On the other hand, considering the UV penetration depth of about 100 nm in ZnO, the top ZnO layers thicker than about 100 nm in the double-stage PnC can totally absorb the UV illumination and prevent the bottom ZnO layer from being affected by the external stimulation. Moreover, we approximate the conductivity modulation through the top ZnO layer thickness to be uniform.

Figures 3(a) and 3(b) show the band structures of the double-stage PnC [Fig. 1(a)] with $h_u = 150$ nm for the lower ($\sigma_u = 0$) and upper ($\sigma_u = \infty$) extreme conductivity limits of the top ZnO layer. It is notable that we assume the conductivity of the bottom bare ZnO layer to be fixed at $\sigma_d = 0$ regardless of external stimulation. As it is shown in Figs. 3(a) and 3(b), when σ_u is increased from 0 to ∞, nearly all the surface modes are downshifted by about 100 MHz without any other significant variation, which is in agreement with our previous results on the line-defect guiding modes in a single-stage PnC [14]. Figure 3(c) shows the total displacement for the points *A, B, C, D, E,* and *F* in Fig. 3(a), wherein *A, C, D,* and *E* correspond to different surface modes at the *X* point, and the corresponding displacements are mostly confined around the two ZnO layers and pillar. *F* corresponds to a bulk mode at the *X* point, in which the elastic energy is mostly spread through the substrate. Points B_1–B_4 show the intersection of the surface-coupled bands with the horizontal dashed line in Fig. 3(a), revealing simultaneous excitation of the corresponding eigenmodes [Fig. 3(c)] for the incident excitation frequency of 5 GHz. It can also be observed in Fig. 3(c) that the elastic energy can be localized in the top ZnO layer (point *A*), the bottom ZnO layer (point *D*), the top and bottom ZnO layers (point *C*), and both the ZnO layers and pillar (point *E*), depending on the incident frequency. Figures 3(d) and 3(e) show the displacement components for modes B_1 and B_2, wherein *x* and *z* displacement components are dominant for sagittal-polarized modes like B_1 and the *y* component is dominant for a shear-polarized mode like B_2. These data are in agreement with the presented sagittal-to-shear ratio depicted by band colors in the band structures. Moreover, Figs. 3(f) and 3(g) show the total displacement profiles relating to constant frequencies of 8 and 10.5 GHz in Fig. 3(a), revealing three and two excited surface modes, respectively. Using two-dimensional (2D)
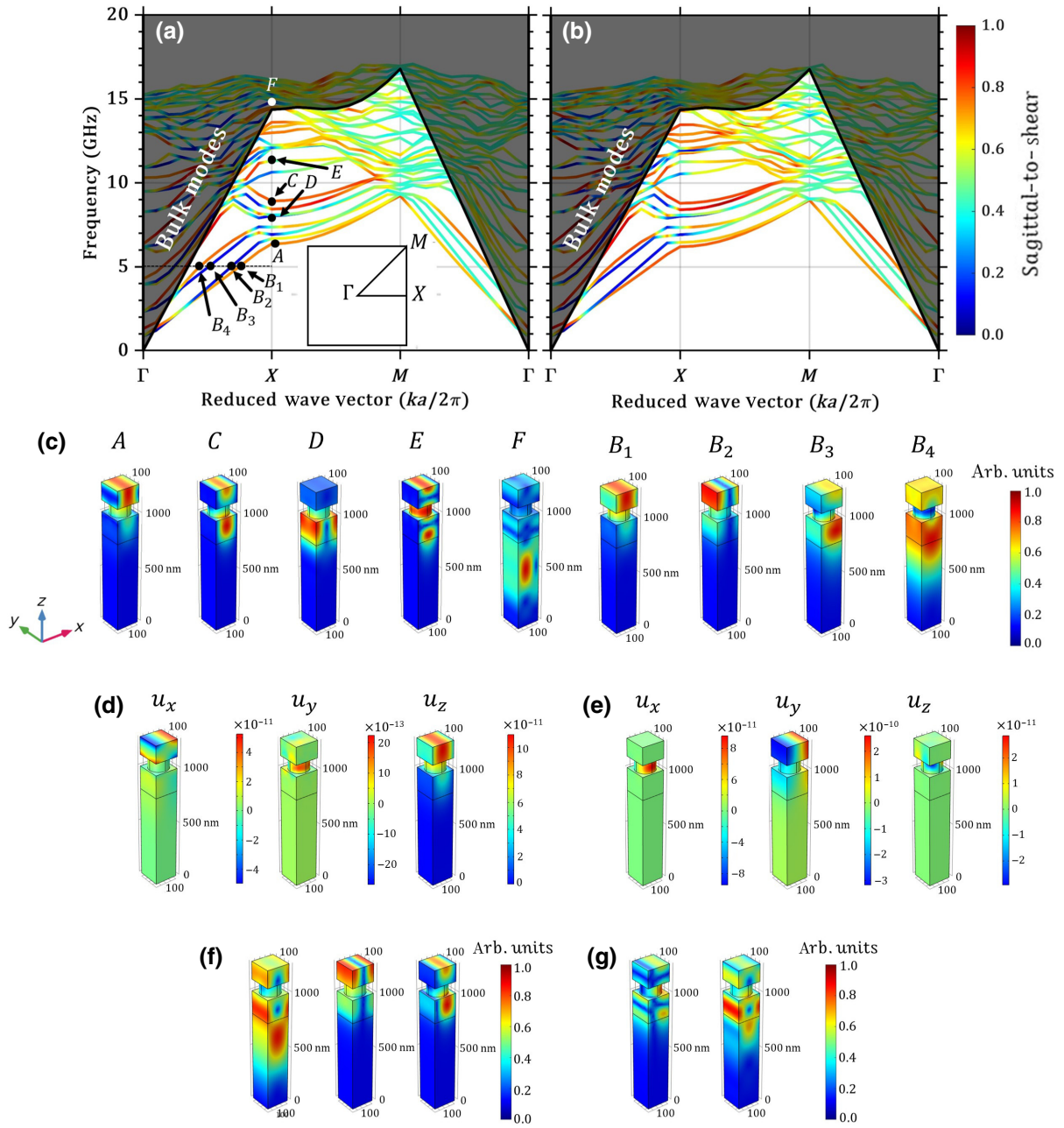
FIG. 3.   (a),(b) Band structures corresponding to the unit cell of double-stage PnC with $\sigma_u = 0$ and $\sigma_u = \infty$, respectively. (c) Total displacement profiles corresponding to points A–F shown in (a). (d),(e) Displacement components corresponding to the eigenmodes of point B_1 and B_2, respectively. Total displacements at constant frequencies of (f) 8 GHz and (g) 10.5 GHz in (a), decomposed to different surface-coupled eigenmodes.

pillar-based PnCs opens the opportunity for implementing the proposed 2D double-stage PnC with various designs, which can allow high degrees of freedom for elastic wave manipulation and routing, including selective coupling of the incident wave to the upper and bottom guiding layers, while rotating the propagation direction and converting the polarization simultaneously. However, if we aim for just the coupling effect of the incoming elastic wave to different paths, we can apply a one-dimensional double-stage PnC,

consisting of a Si grating (along the x axis) instead of pillars, and achieve similar displacement profiles at slightly different frequencies.

Based on the results in Fig. 3, we can select for desirable behaviors of the proposed double-stage PnC among the different possible applications. To design a vertical SAW splitter with the capability of dividing the elastic energy into the top and bottom ZnO layers, eigenmodes of point C in Fig. 3(a) should be excited so that SAW waves can
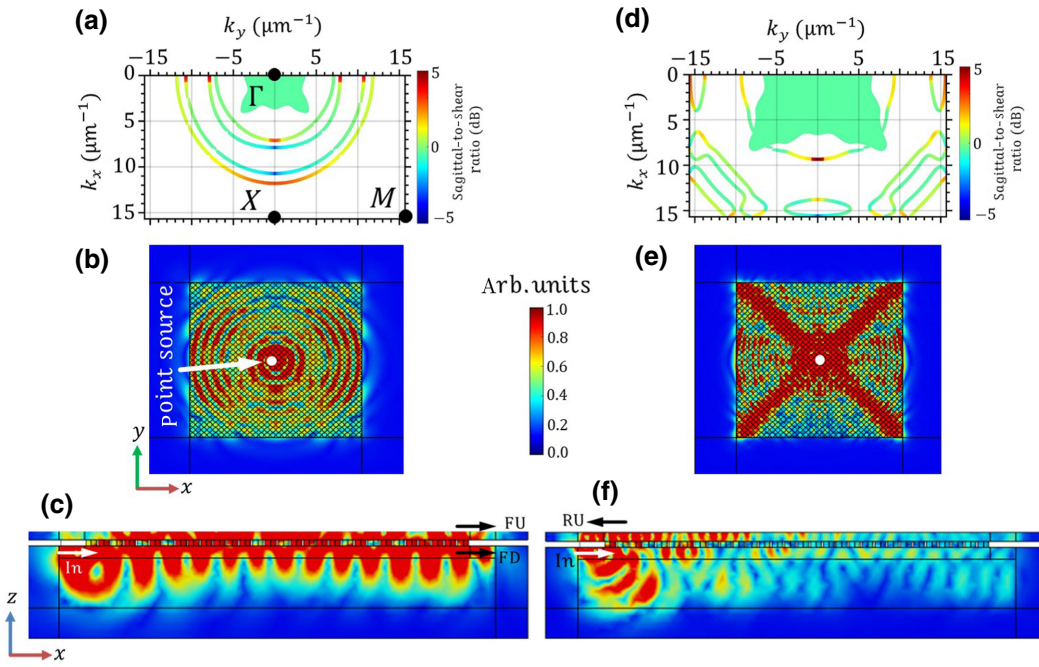
FIG. 4. (a) Isofrequency contours of the unit cell in Fig. 2(j) at 5 GHz. (b) Propagation of elastic wave in the bottom ZnO layer as a consequence of a sagittal-polarized point source, assumed at the surface of the bottom ZnO layer (shown by the white dot). (c) Total displacement profile of the supercell along Γ-X direction for sagittal line source at 5 GHz. Parts (d)–(f) display the same content as parts (a)–(c), but at constant incident frequency of 8 GHz.

propagate in both the top and bottom ZnO layers along the x direction. Eigenmodes like point A and D support SAW propagation in one of the ZnO layers dominantly, so that their excitation can be used for efficient coupling of the elastic wave from one layer to another. This application can lead to alternative vertical acoustic via (analogue of electric via), in applications like active acousto-optic components in integrated photonic chips.

To elaborate the presented double-stage PnC behavior, we plot the isofrequency contours at $\sigma_u = 0$, for 5 and 8 GHz in Figs. 4(a) and 4(d). The isofrequency plots are obtained through calculation of eigenfrequencies for all possible combinations in the k_x-k_y plane, and finding their intersections with constant frequencies. The color in these isofrequency contours denotes the sagittal-to-shear polarization ratio at that point, and the filled green regions correspond to the bulk modes. Γ, X, and M show the high symmetry points of the first Brillouin zone in Fig. 4(a), and the displayed data in this figure are in complete agreement with the discussed band structure in Fig. 3(a). Figures 4(b) and 4(e) show the elastic wave propagation from a central sagittal point source on the bottom ZnO layer in the presented double-stage PnC, wherein we assume 30 rows of pillars in both the x and y directions. These figures display the in-plane (x-y plane) displacement profiles on the surface of the bottom ZnO layer, which are similar to the displacement distributions on the top ZnO layer. It can be obviously observed in Fig. 4(c) that sagittally excited

elastic waves propagate nearly isotropically at 5 GHz, which is consistent with Fig. 4(a). At 8 GHz, Fig. 4(d) reveals a band with negative group velocity around the X point along the Γ-X direction, which can lead to a suppressed elastic wave propagation along the x direction, as shown in Fig. 4(e), in which the elastic wave is completely focused in the Γ-M direction. Figures 4(c) and 4(f) demonstrate the cross section (x-z plane) of the total displacement of the corresponding supercells with sagittal line sources along the x direction at 5 and 8 GHz, respectively. Here, the input line source and the forward ($+x$ direction) output on the top and bottom layers are labeled as In, FU, and FD, respectively. Figure 4(c) demonstrates the excited elastic waves propagating along the $+x$ direction in both the top and bottom ZnO layers at 5 GHz. However, Fig. 4(f) reveals the dominant elastic wave propagation in the opposite direction ($-x$) through the top ZnO layer at 8 GHz. Here, the reverse output on the top ZnO layer is labeled as RU. Therefore, the proposed double-stage PnC has the capability to guide different surface-coupled modes anisotropically through excitation of different eigenmodes, depending on polarization and frequency.

Figure 5(a) depicts the reduced band structure of the double-stage PnC [unit cell in Fig. 1(a)] in the Γ-X direction beside the calculated shear transmissions through the output ports of the corresponding supercell [Fig. 1(b)]. Both band structure and transmission calculations are

carried out for $\sigma_u = \sigma_d = 0$, when there is no external stimulation. Here, we assume a shear input line source at the In cut line and calculate the transmission spectra corresponding to the output forward transmissions on the bottom (FD) and top (FU) ZnO layers in the $+x$ direction, and the reverse transmission on the top ZnO layer in the $-x$ direction (RU). Individual transmission spectra in Fig. 5(a) reveal that the input elastic wave can be coupled to either the top or bottom ZnO layer at each excitation frequency.

The top and bottom ZnO layers behave like elastic waveguides that are coupled through the pillars, so that they periodically exchange elastic energy during wave propagation along the x direction. This elastic energy exchange can be observed in Figs. 5(b)–5(g), depicting the total displacement profiles of the supercell in the cross-section views (x-z plane). Figures 5(b) and 5(c), 5(d) and 5(e), and 5(f) and 5(g) correspond to incident frequencies of 5, 8, and 10.5 GHz, respectively. Here, we assume 11 pillars
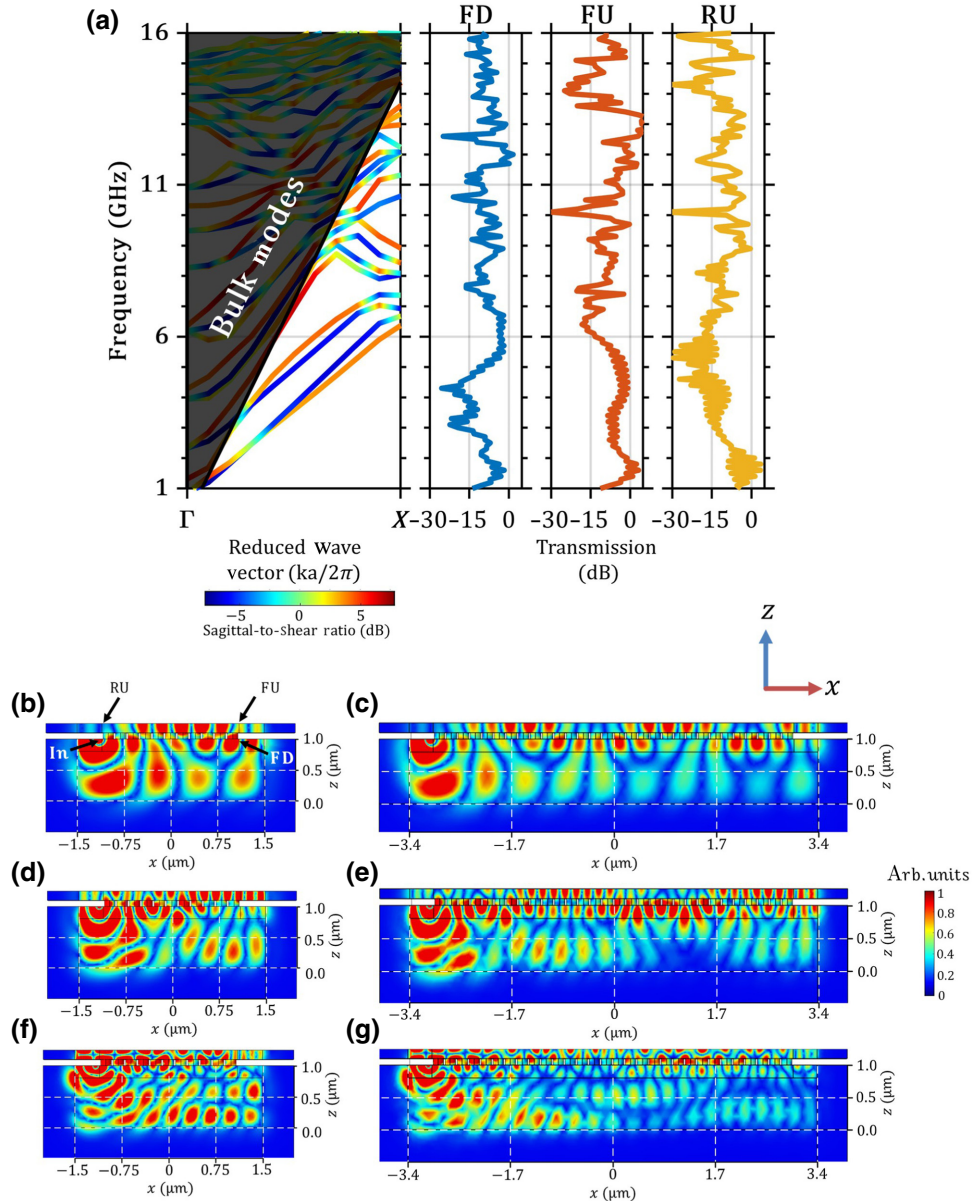

FIG. 5. (a) Band structure of the unit cell in Fig. 1(a) along Γ-X direction beside the transmission spectra of the corresponding supercell [Fig. 1(b)] in the forward ($+x$) direction on the bottom (FD) and top (FU) ZnO layers, and in the reverse ($-x$) direction on the top ZnO layer (RU). Output ports corresponding to transmission spectra of FD (blue spectrum), FU (red spectrum), and RU (orange spectrum) are highlighted in (b). (b),(d),(f) Total displacement distributions in the cross-section views (x-z plane) of the supercell with 11 pillar rows along x direction at incident frequencies of 5, 8, and 10.5 GHz, respectively. (c),(e),(g) The same content as parts (b),(d),(e), but with 30 rows of pillars along x direction in the supercell.

in Figs. 5(b), 5(d), and 5(f), and 30 pillars in Figs. 5(c), 5(e), and 5(g) along the x axis, proving that increasing the coupled elastic propagation length can switch the outward elastic energy from FD to FU, or vice versa.

The sinusoidal profile of the coupling between the top and bottom ZnO waveguides is obviously observed in further propagation lengths of coupled elastic waveguides, such as Figs. 5(c), 5(e), and 5(g). Figures 5(b) and 5(c) [Figs. 5(d) and 5(e)] show the coupled elastic wave propagation at 5 GHz (8 GHz). Moreover, there are some specific lengths that the elastic waves can propagate in both top and bottom waveguides simultaneously with a slight transmission difference of about 1 dB (FD $= -8.8$ dB and FU $= -9.9$ dB), as shown in Fig. 5(e) for 30 pillars at 8 GHz. This configuration case can serve as a vertical elastic splitter, which is used in the next section of this work to design a supersensitive vertical Mach-Zehnder device. Hence, the dominant output port in elastic energy transmission depends on the number of pillars (coupled elastic propagation length) and the excitation frequency. In Figs. 5(f) and 5(g), it can be observed that elastic waves are mostly reflected from the top ZnO layer at 10.5 GHz, so that the dominant output transmission at RU is independent of the pillar number. In general, based on Figs. 3–5 the routing propagation path of the elastic wave in the proposed vertical PnC can be controlled by geometrical parameters, such as pillar dimensions and number of pillars along the propagation direction, and incident wave properties, such as polarization and frequency.

The assumed shear horizontal line source in the transmission calculations is allowed to couple to the top or bottom ZnO waveguides without imposing significant polarization change, owing to the assumed PBCs along the y direction in the investigated supercell [Fig. 1(b)]. In other words, we expect that the assumed supercell fully supports the polarization of the shear excitation, because the purely y-directed source displacements are not exposed to

any confinement along the y direction in the supercell (see Fig. 11 in the Appendix).

IV. THE PROPOSED VERTICAL MACH-ZEHNDER DEVICE

The proposed supersensitive elastic Mach-Zehnder device, based on the discussed double-stage PnC as the vertical SAW splitter, is shown in Fig. 6(a). It can be observed that the proposed device includes a Si substrate, a bottom ZnO layer on the substrate, a double-stage PnC consisting of 5×11 Si pillars in the x-y plane, and a top ZnO layer. The shear-polarized SAW is assumed to be excited on the surface of the bottom ZnO layer, while the output detection port is assumed to be on the top ZnO layer, as shown in Fig. 6(a). Because of the vertical nonplanar design of the structure, only the top ZnO layer is affected by the external stimulation, leading to a consequent modulation of σ_u. The proposed nonplanar SAW Mach-Zehnder design, with the top ZnO layer as a thin sensing layer, benefits from a small chip area and a supersensitive sensing behavior, without requiring local focusing of the external stimulation (e.g., UV illumination) on the sensitive branch, as compared with the conventional planar Mach-Zehnder configurations. Moreover, here we do not need an extra dummy SAW device as the reference in conventional differential measurements, and highly sensitive real-time sensing with minimal cross sensitivity can be achieved in a single double-stage Mach-Zehnder configuration.

Figure 6(b) shows the cross-section scheme of the proposed structure, along the dashed line (AA') in Fig. 6(a). Figure 6(b) illustrates the typical parts of a Mach-Zehnder device, consisting of the splitting PnC region to divide the incoming SAW into the top and bottom ZnO-based waveguides, the phase region wherein the elastic properties of the top branch are modulated individually by the external stimulation, and the interference region wherein the top and
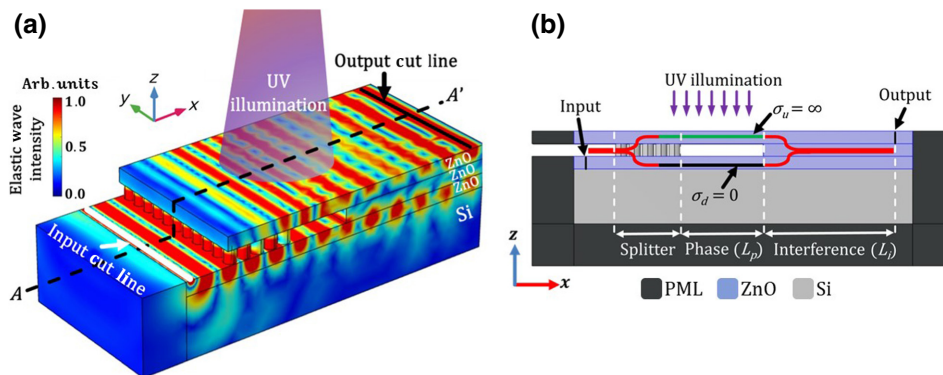

FIG. 6. (a) Schematic view of the proposed vertical SAW Mach-Zehnder device, in which the double-stage PnC zone splits the incident SAW into the top and bottom ZnO layers. The top ZnO layer is exposed to external stimulation such as UV illumination. Elastic waves from both the top and bottom ZnO layers interfere to realize the output SAW. (b) Schematic cross-section structure of the device presented in (a), wherein the splitter zone, the phase zone, and the interference zone are shown.

bottom elastic waves interfere, producing the output signal at the end. It is notable that the elastic properties of the top ZnO layer are supposed to be modulated based on the AE effect and the resulting modulation of effective stiffness matrix elements with the conductivity modulation, which in turn is a consequence of external stimulation. As shown in Fig. 6(b), elastic waves propagate along a length of L_p in the phase region, affecting the total phase difference between the top and bottom branches, and consequently the final output signal. Moreover, replacing the isolating air gap between the top and bottom ZnO layers by an intermediate ZnO film, we make the elastic branches merge in the interference region with length of L_i, and define the output probe at the end of this region. It is notable for each design set of geometrical parameters of the double-stage PnC (as in Table I), we can achieve different optimized L_p and L_i values for the proposed Mach-Zehnder device. Therefore, we assume the geometrical parameters of the Mach-Zehnder device according to Table I, and then optimize L_p and L_i. It should be noted that we assume the thickness of the intermediate ZnO layer in the interference region to be equal to the height of the Si pillars, as shown in Fig. 6, to achieve a feasible and well-defined device structure.

Another consideration is that L_p not only determines the phase difference between top and bottom ZnO layers, but also changes the splitter behavior through varying the input acoustic impedance that is seen after that. The acoustic impedance of the top and bottom ZnO layers, seen from the splitter end, are dependent on the waveguide geometry (L_p and yz cross-section area), material density, and wave velocity [33]. The same impedance issue should be considered for the affecting parameters of the interference region (L_i and yz cross-section area), which can lead to elastic reflections from the phase-interference interface at the top and bottom branches. Therefore, L_p and L_i have significant effects on the behavior of their previous stages and, consequently, the total device. Regarding this, we optimize the values of L_p and L_i in the complete Mach-Zehnder structure to achieve the highest extinction ratio at the output cut line.

It is evident that longer elastic wavelengths need longer L_i values to achieve a well-defined interference pattern. Moreover, the L_i value modulates the acoustic impedance of the interference region at the phase-interference interface. In accordance with the latter discussions, simulation results (see Fig. 12 in the Appendix) show that the operational frequency of the proposed Mach-Zehnder structure shifts to frequencies higher than about 9 GHz for $L_i = 5$ μm, while for $L_i = 10$ μm the highest extinction ratio is achieved at about 4 GHz. Therefore, we consider $L_i = 10$ μm to assure a successful Mach-Zehnder behavior in the 1–10 GHz range, then optimize the L_p value.

To optimize L_p in the proposed Mach-Zehnder device, first we investigate the transmission values of the

corresponding supercell with finite dimension along the x axis at the two extreme limits of the top ZnO layer conductivity corresponding to transmission values of T_0 and T_∞: (i) $\sigma_u = 0$ for the absence of external stimulation, and (ii) $\sigma_u = \infty$ for the intensive presence of external stimulation. To achieve the maximum sensitivity of the designed Mach-Zehnder device, L_p is optimized so that the resulting extinction ratio [$|10 \times \log_{10}(T_\infty/T_0)|$] is maximized, wherein the output signal changes significantly by exposure to external stimulation. Moreover, we pick up designs in which both extinction ratio and maximum transmission [max(T_0, T_∞)] value are maximized simultaneously, so that we can achieve a highly sensitive device in addition to an acceptable and measurable output signal. Figure 7(a) shows the calculated extinction ratios of the proposed SAW Mach-Zehnder supercell [Fig. 6(b)], with varying phase region length (L_p) from 50 to 6000 nm, and incident frequency for $L_i = 10$ μm. For lower operation frequencies in Fig. 7(a), a periodic dependence of the extinction ratio on L_p can be obviously observed at each frequency. For more clarification, Fig. 7(b) depicts T_∞ versus L_p at three different frequencies of 1 GHz (bottom), 2 GHz (middle), and 3 GHz (top), shown by horizontal dashed lines in Fig. 7(a). As expected from the periodic nature of the produced phase delay in the top ZnO layer, the observed periods in this part grow shorter for higher incident frequencies. This figure confirms that the interference effect is dominantly responsible for the observed periodic variations of the extinction ratio. The phase of the elastic wave at the bottom ZnO layer that propagates with a velocity of c_1 after a length of L_p is $\varphi_1 = 2\pi L_p f / c_1$, where f is frequency. For the top ZnO layer, the phase is $\varphi_2 = 2\pi L_p f / c_2$, wherein c_2 is the elastic wave velocity along the top ZnO layer. The velocities c_1 and c_2 are mainly dependent on the conductivity value that modulates the effective elastic matrix, based on Eq. (9), as well as dimensions and boundary conditions of the ZnO layers. Constructive interference occurs when $|\Delta\varphi| = |\varphi_1 - \varphi_2| = 2m\pi$, where m in an integer, leading to two adjacent maxima of T_∞ with a period of ΔL_p,

$$\Delta L_p = \frac{1}{f \, |(1/c_1) - (1/c_2)|}. \tag{11}$$

However, it should be noted that L_p is not the only parameter that determines the elastic wave phase and amplitude, and the input acoustic impedances affect the final transmission values too. However, considering Eq. (11) we can estimate ΔL_p values with an error of about $\pm 10\%$ at each frequency in Fig. 7(b).

To optimize the final Mach-Zehnder device with finite dimensions along both the y and x axes, again we assume $L_i = 10$ μm, and reoptimize the L_p value. Here, we use the configuration shown in Fig. 6(a) to carry out three-dimensional simulations. Geometrical parameters are set
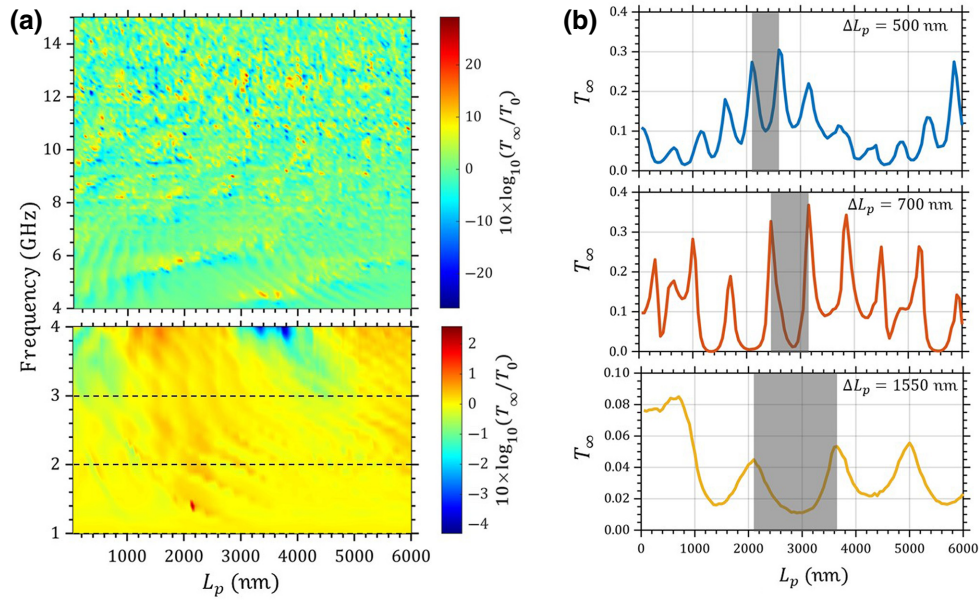
FIG. 7. (a) Variation of the extinction ratio $10 \times \log_{10}(T_\infty/T_0)$ of the proposed Mach-Zehnder device versus varying incident frequency and phase zone length (L_p) for $L_i = 10$ μm. (b) Calculated T_∞ versus varying L_p at frequencies of 3 GHz (blue curve), 2 GHz (red curve), and 1 GHz (orange curve).

according to Table I, while the double-stage PnC consists of 5 pillar rows along the x axis, and 11 pillar rows along the y axis. Figure 8 depicts the calculated extinction ratios with varying incident frequency from 1 to 10 GHz and L_p from 50 to 5000 nm with a step of 50 nm. Among the observed hot spots in this plot, $L_p = 1650$ nm leads to both maximum extinction ratio of 23.5 dB and output signal of -8 dB for the complete finite design at 8.6 GHz. Moreover, the periodic variation of extinction ratios with varying L_p can be observed in Fig. 8.

Figure 9(a) shows the T_0 (solid blue) and T_∞ (dashed red) transmission spectra of the designed complete device for $L_p = 1650$ nm, confirming output signal of $T_0 = -8$ dB, and extinction ratio of 23.5 dB at extreme variation limits of σ_u at 8.6 GHz. Figures 9(b) and 9(c) exhibit the total displacement cross-section (x-z plane) profiles corresponding to T_0 and T_∞, respectively. Again, Figs. 9(b) and 9(c) show the lag between the elastic waves, which originates from different phases of elastic waves at the top ZnO layer. This AE-induced phase difference leads to different interference profile patterns in Figs. 9(b) and 9(c), and thus the observed high extinction ratio. On the other hand, the displacement profiles reveal that the splitting behavior of the double-stage PnC and the coupling strength to the top and bottom ZnO layers are also affected by external stimulation and the related conductivity modulation. These elastic wave profiles show that external stimulation leads to a decrease in the elastic coupling strength of the incident wave to the top ZnO layer for T_∞. This splitting modulation behavior is attributed to the aforementioned downshift of surface bands of the double-stage PnC, as in Figs. 3(a)

and 3(b), when increasing σ_u from 0 to ∞. In other words, T_0 shows a high transmission level due to constructive interference of the top and bottom elastic waves, and the superficial confinement of elastic energy in the vicinity of the output surface probe. Similarly, T_∞ shows a low transmission level because of the destructive interference of the elastic waves propagating in the top and bottom waveguides, and the weak elastic coupling to the top ZnO layer for $\sigma_u = \infty$. Moreover, it is notable that the elastic wave
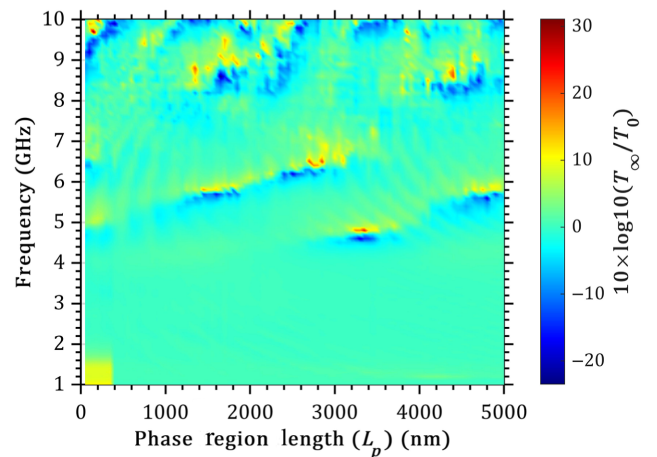

FIG. 8. Variation of transmission extinction ratio of the final finite Mach-Zehnder device with 5×11 pillars in the x-y plane versus varying incident frequency and length of the phase zone in the proposed supersensitive elastic device. Here, $L_i = 10$ μm.
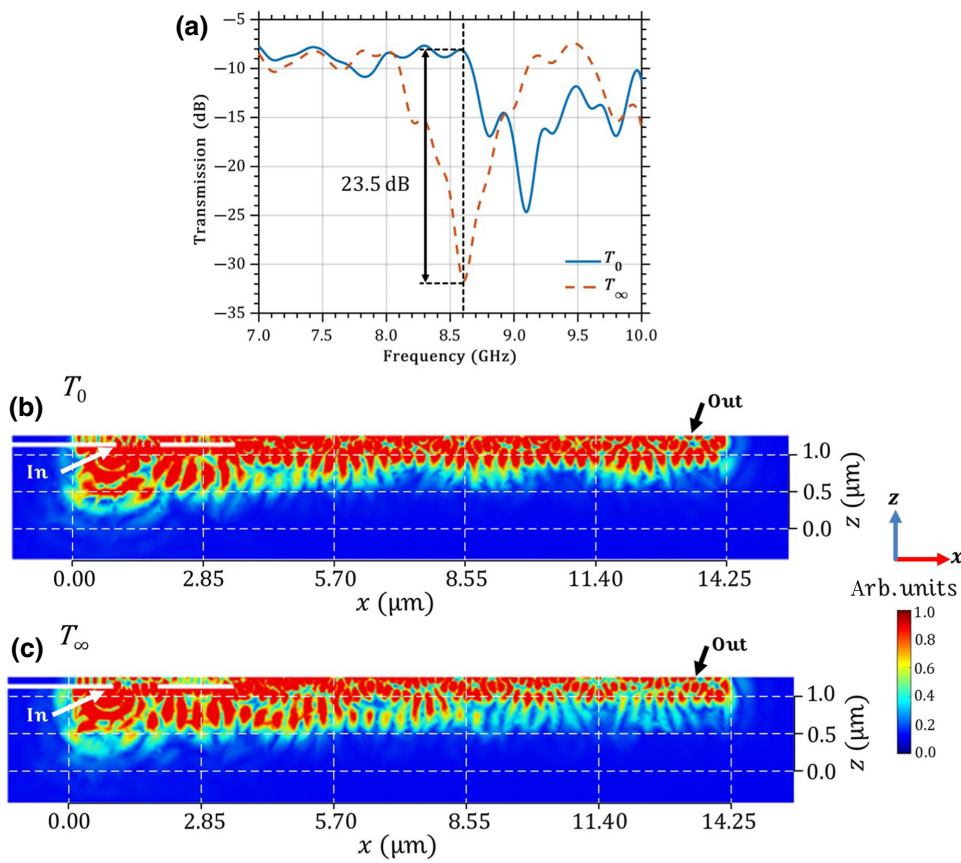
FIG. 9. (a) Spectra of the designed finite Mach-Zehnder device with 5×11 pillars in the x-y plane and $L_i = 10$ μm and $L_p = 1.65$ μm, in the absence (T_0) and presence (T_∞) of external stimulation. (b),(c) Total displacement profiles at incident frequency of 8.6 GHz, corresponding to T_0 and T_∞, respectively. The incident source is assumed shear polarized.

vector at the phase-interference interface is deflected to a finite angle from the x axis due to the different effective acoustic impedances, in addition to the asymmetric wave incidence versus the ZnO guiding layer thickness in the interference region. Therefore, the elastic wave enters the interference region at a finite angle with respect to the x axis, which leads to propagation, while experiencing total internal reflections from the top and bottom interfaces (with Si substrate) of the ZnO layer. This behavior can be observed more clearly in propagation patterns along the x

axis in the supercell simulations [Figs. 13(b) and 13(c)], which are in accordance with Figs. 9(b) and 9(c).

To elaborate the sensitivity of the designed Mach-Zehnder device, we vary σ_u from 10^{-3} S/m to 10^4 S/m, and calculate the corresponding output transmission spectra ($T_{\sigma u}$). Figure 10(a) shows $10 \times \log_{10}(T_{\sigma u})$ spectra for different σ_u values, revealing that the larger σ_u leads to a smaller transmission value at 8.6 GHz. Figure 10(b) shows the variation trend of transmission values with varying σ_u at 8.6 GHz. It is observed that increasing σ_u in the
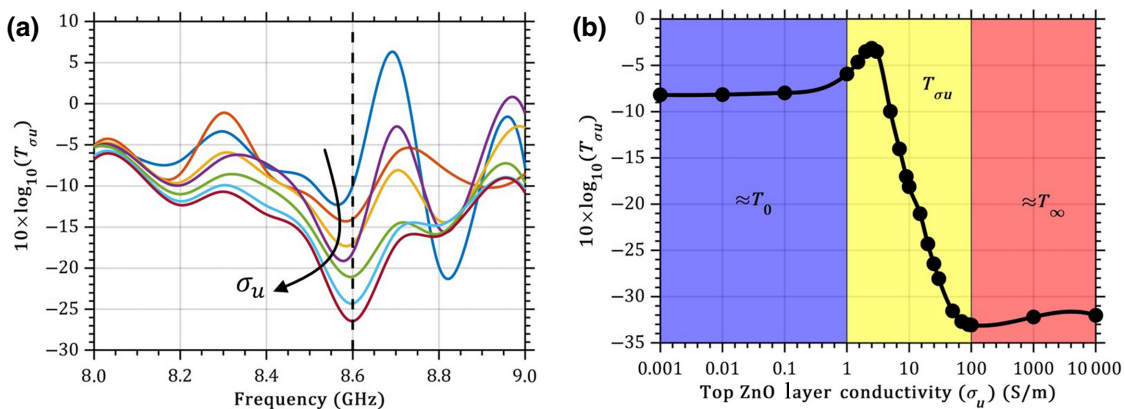

FIG. 10. (a) Transmission spectra [$10 \times \log_{10}(T_{\sigma u})$] of the designed vertical Mach-Zehnder device for different values of conductivity of the top ZnO layer (σ_u). (b) Variation of $10 \times \log_{10}(T_{\sigma u})$ versus σ_u at the fixed frequency of 8.6 GHz.
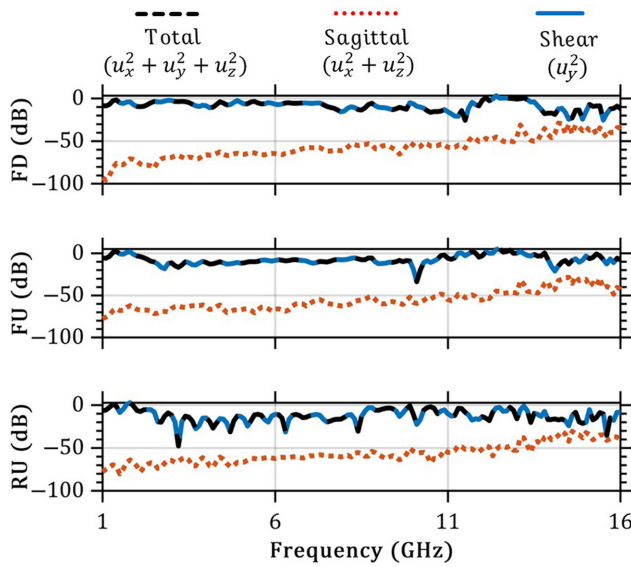
FIG. 11.   Total transmission spectra $(u_x{}^2 + u_y{}^2 + u_z{}^2)$ (dashed black spectra) of FD, FU, and RU in Fig. 5(a), each decomposed to sagittal $(u_x{}^2 + u_z{}^2)$ (dotted red) and shear $(u_y{}^2)$ (solid blue) spectral components, when polarization of the source is assumed shear.

low-conductivity regime up to 1 S/m (violet zone) does not change $T_{\sigma u}$ significantly from being approximately equal to T_0. Similarly, increasing σ_u from about 100 S/m toward higher conductivity levels (pink zone) does not change the $T_{\sigma u}$ value considerably and it remains about equal to T_∞. However, for 2.5 S/m $< \sigma_u <$ 50 S/m (yellow zone), the $T_{\sigma u}$ value reveals a nearly linear correlation to σ_u with an output sensitivity of about 0.63 dB/(S/m). The observed variation trend in Fig. 10(b) is in good agreement with the conventional trend of SAW-velocity modulation by conductivity reported in the literature [14,34]. Moreover, this trend is consistent with the conductivity-induced modulation of the defect mode guiding frequencies in a single-stage PnC in our previous work [14]. Here, we propose and design a nonplanar SAW Mach-Zehnder device based on double-stage PnCs, and explore the related physical operation behavior. Moreover, we propose this configuration as a highly sensitive sensor in response to external stimulations, and evaluate the related sensing performance.

Considering the vertical design of the proposed elastic Mach-Zehnder device, external stimulations such as UV light can only affect the conductivity of the top ZnO layer. However internal disorders may deteriorate the extinction ratio of the designed device. Therefore, we evaluate the performance of the proposed elastic Mach-Zehnder device with respect to the variation of geometrical and material parameters, such as pillars' radius, permittivity, and elastic matrix elements (C) of the ZnO thin films. To maintain a definite high extinction ratio ($\geq$20 dB) at a frequency of 8.3 GHz, the maximum acceptable tolerance in pillars'

radius is in the range of -0.5% to $+4\%$ around 85 nm. Moreover, it is notable that the maximum acceptable tolerance of relative permittivity is achieved in the range of -3.23% to $+1.52\%$, while the tolerance of the elastic matrix components is in the range of -1.33% to $+0.57\%$ in the ZnO layers.

V. CONCLUSION

In this report, we propose a vertical SAW Mach-Zehnder device that benefits from a double-stage PnC, consisting of Si pillars sandwiched between two ZnO layers. This structure can route the incident SAWs into different ports depending on incident frequency and polarization. Here, we design the double-stage PnC as an efficient vertical splitter for the incident SAW, dividing the incident elastic wave into the suspended top and the bottom ZnO waveguides. We propose the designed vertical Mach-Zehnder device as a highly sensitive sensor for detecting external stimulations such as UV illumination or hydrogen exposure. The suspended top ZnO layer serves as the sensing branch in the proposed Mach-Zehnder design, in which elastic wave propagation is modulated through the AE effect in response to external stimulation. Moreover, the bottom ZnO layer serves as the reference branch, which is inherently protected from external stimulation due to the vertical structure of our design. This protection prevents additional complication to exert local stimulation on the sensing branch, as in conventional planar Mach-Zehnder structures. It is proved that the proposed highly sensitive SAW Mach-Zehnder design leads to an extinction ratio of 23 dB when increasing the conductivity of the top ZnO layer from about 1 S/m to 100 S/m. Based on the presented results, the proposed highly sensitive double-stage device may be a promising candidate for sensing applications such as real-time detection of UV illumination or hydrogen exposure.

APPENDIX: SUPPLEMETARY SIMULATIONS

This appendix shows some other useful simulations to validate the assumptions and optimizations of the proposed vertical Mach-Zehnder device. In Fig. 11 we explore the polarization behavior by superimposing the calculated total output transmission spectra $(u_x{}^2 + u_y{}^2 + u_z{}^2)$ at FD, FU, and RU onto the separated sagittal $(u_x{}^2 + u_z{}^2)$ and shear $(u_y{}^2)$ transmission components, in response to a shear-polarized source in the supercell [Fig. 1(b)]. According to Fig. 11, sagittal components are negligible and
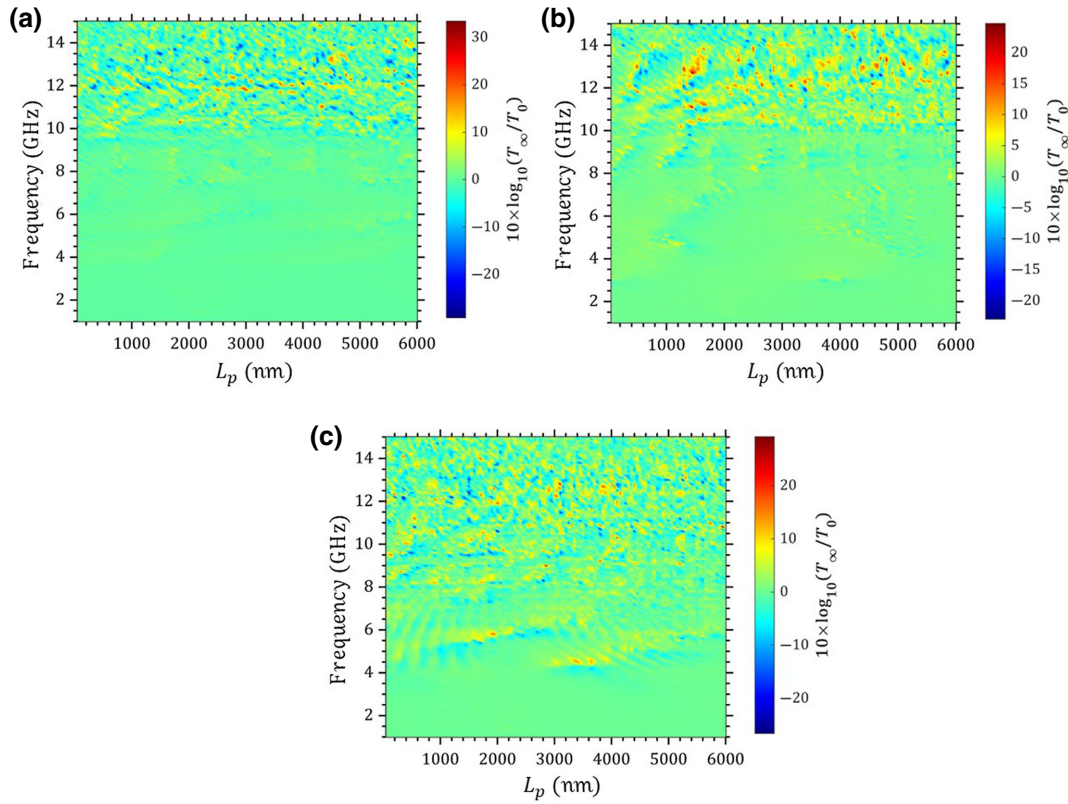
FIG. 12. Variation of the extinction ratio $10 \times \log_{10}(T_\infty/T_0)$ of the proposed Mach-Zehnder device versus varying incident frequency and phase zone length (L_p) at different interference zone lengths of (a) $L_i = 2$ μm, (b) $L_i = 5$ μm, and (c) $L_i = 10$ μm.

all outputs keep the shear polarization in all frequencies, without any significant polarization exchange.

To optimize L_p and L_i values in the proposed Mach-Zehnder device, Figs. 12(a)–12(c) show the calculated extinction ratios of the proposed SAW Mach-Zehnder supercell [Fig. 6(b)], versus varying the phase region length (L_p) from 50 to 6000 nm, and incident frequency for different interference region lengths of $L_i = 2$, 5, and 10 μm, respectively. As it is shown in Fig. 12, higher L_i values lead to the extension of high extinction ratios and operation frequency range into the lower frequencies. This observation is attributed to elastic impedance modulation of the interference region by varying L_i, so that impedance matching can occur at $L_i = 10$ μm, which minimizes the elastic reflections at the phase-interference interface and allows well-behaved interference of elastic waves in the interference region. Moreover, for lower operation frequencies in Fig. 12(c), a periodic dependence of the extinction ratio on L_p can be obviously observed at each frequency.

Moreover, considering extinction ratio hot spots in Fig. 12(c), we choose $L_p = 2.8$ μm at 8.3 GHz for our highly sensitive Mach-Zehnder design to achieve the highest possible output signal [max(T_0, T_∞)], as well as a high extinction ratio. Figure 13(a) indicates the resulting

T_0 (solid blue) and T_∞ (dashed red) transmission spectra of the supercell, revealing a high transmission contrast of about 21 dB, and a high output signal of -1.5 dB at a frequency of 8.3 GHz. Figures 13(b) and 13(c) show the total displacement distributions in the supercell at 8.3 GHz, corresponding to T_0 and T_∞, respectively. As shown in Figs. 13(b) and 13(c), incident elastic waves are successfully coupled to both top and bottom waveguides in the splitter regions, propagate through the same length but with different phase delays along the phase regions, then merge and interfere in the interference regions with different profiles, leading to an extinction ratio of about 21 dB at a fixed output probe (shown by Out). Vertical dashed lines at some specific x positions in Figs. 13(b) and 13(c) clarify the observed elastic wave lag between the unstimulated and stimulated conditions after the phase regions, which originates from the phase delay difference induced by external stimulation. Thus, our optimized design leads to the maximum output sensitivity of about 21 dB for the investigated supercell in response to extreme limits of external stimulations ($\sigma_u = 0, \infty$). Comparing Figs. 13(a) and 9(a), an enhancement of 2.5 dB is observed in the extinction ratio of the optimized device with finite dimensions versus the optimized supercell design. This subtle enhancement is attributed to the elastic splitting
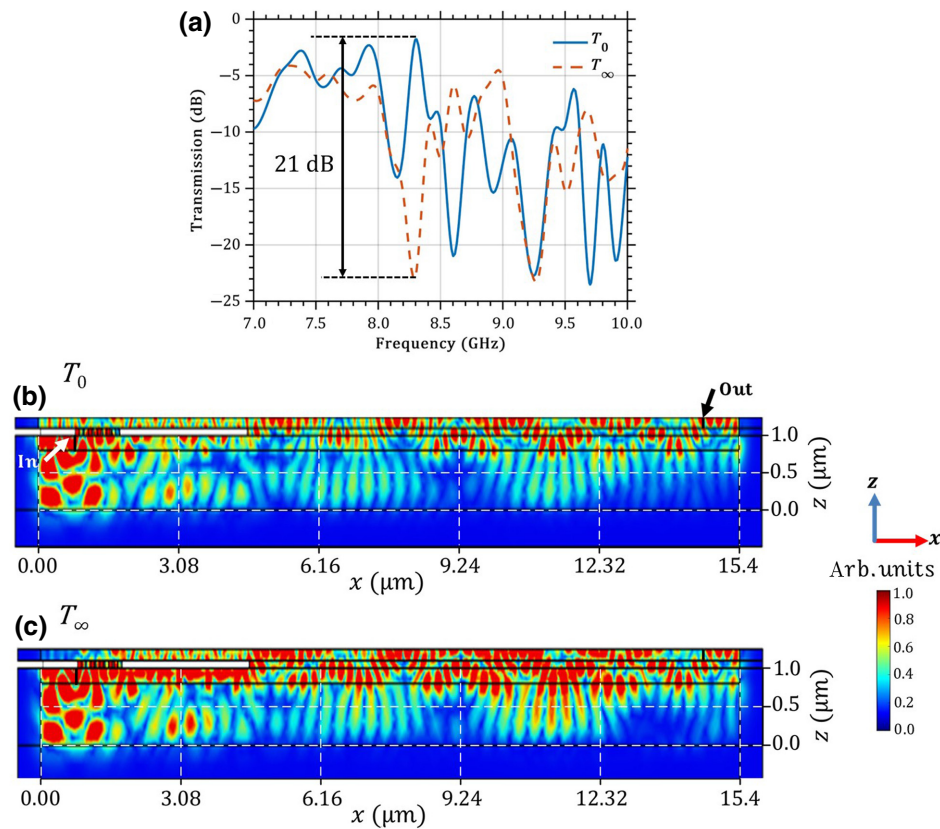
FIG. 13. (a) Transmission spectra of the supercell with interference zone length of $L_i = 10$ μm and phase zone length of $L_p = 2.8$ μm in the absence of external stimulation (T_0, solid blue spectrum) when $\sigma = 0$, and in the presence of extreme external stimulation (T_∞, dashed red spectrum) when $\sigma = \infty$. (b),(c) Total displacement distributions at incident excitation frequency of 8.3 GHz, corresponding to T_0 and T_∞, respectively. Incident polarization of the source is assumed shear.

modulation by varying σ_u, which can be dependent on the L_p value of the design.

[1] D. P. Morgan, A history of surface acoustic wave devices, Int. J. High Speed Electron. Syst. **10**, 553 (2000).

[2] J.-Y. Duquesne, P. Rovillain, C. Hepburn, M. Eddrief, P. Atkinson, A. Anane, R. Ranchal, and M. Marangolo, Surface-Acoustic-Wave Induced Ferromagnetic Resonance in Fe Thin Films and Magnetic Field Sensing, Phys. Rev. Appl. **12**, 024042 (2019).

[3] C. Wang, C. Wang, D. Jin, Y. Yu, F. Yang, Y. Zhang, Q. Yao, and G.-J. Zhang, AuNP-amplified surface acoustic wave sensor for the quantification of exosomes, ACS Sens. **5**, 362 (2020).

[4] M. M. Mehrnegar, S. Darbari, and M. K. M. Farshi, Simulating a graphene-based acousto-plasmonic biosensor to eliminate the interference of surrounding medium, Opt. Express **30**, 15721 (2022).

[5] I. Group, IEEE 5G and Beyond Technology Roadmap White Paper, (2017).

[6] A. Winkler, R. Brünig, C. Faust, R. Weser, and H. Schmidt, Towards efficient surface acoustic wave (SAW)-based microfluidic actuators, Sens. Actuators, A **247**, 259 (2016).

[7] D. A. Golter, T. Oo, M. Amezcua, K. A. Stewart, and H. Wang, Optomechanical Quantum Control of a Nitrogen-Vacancy Center in Diamond, Phys. Rev. Lett. **116**, 143602 (2016).

[8] M. M. Mehrnegar, S. Darbari, H. Ramezani, and M. K. Moravvej-Farshi, Designing graphene-based multi-mode acousto-plasmonic devices, J. Lightwave Technol. **37**, 2126 (2019).

[9] F. Taleb, S. Darbari, and A. Khelif, Reconfigurable locally resonant surface acoustic demultiplexing behavior in ZnO-based phononic crystal, J. Appl. Phys. **129**, 024901 (2021).

[10] F. Taleb, S. Darbari, A. Khelif, and H. Taleb, An acoustoelectric-induced tailorable coupled resonator surface acoustic waveguide, J. Phys. D: Appl. Phys. **54**, 225301 (2021).

[11] R. Sharaf, S. Darbari, and A. Khelif, Nonreciprocity of Gigahertz Surface Acoustic Wave Based on Mode Conversion in an Inclined Phononic Crystal Heterojunction, Phys. Rev. Appl. **16**, 054004 (2021).

[12] A. Hernández-Mínguez, F. Macià, J. Hernàndez, J. Herfort, and P. Santos, Large Nonreciprocal Propagation of Surface Acoustic Waves in Epitaxial Ferromagnetic/Semiconductor Hybrid Structures, Phys. Rev. Appl. **13**, 044018 (2020).

[13] S. Tateno and Y. Nozaki, Highly Nonreciprocal Spin Waves Excited by Magnetoelastic Coupling in a Ni/Si Bilayer, Phys. Rev. Appl. **13**, 034074 (2020).

[14] F. Taleb and S. Darbari, Tunable Locally Resonant Surface-Acoustic-Waveguiding Behavior by Acoustoelectric Interaction in ZnO-Based Phononic Crystal, Phys. Rev. Appl. **11**, 024030 (2019).

[15] M. S. Faiz and N. Abd Aziz, Monochannel demultiplexer phononic crystal slab based on hollow pillars, Crystals **12**, 165 (2022).

[16] J. Babaki and F. Nazari, Heterostructure based demultiplexer using solid–solid phononic crystal ring resonators, J. Phys. D: Appl. Phys. **53**, 375301 (2020).

[17] H. Imanian, M. Noori, and A. Abbasiyan, A highly efficient Fabry-Perot based phononic gas sensor, Ultrasonics **124**, 106755 (2022).

[18] N. Mukhin, M. Kutia, A. Aman, U. Steinmann, and R. Lucklum, Two-dimensional phononic crystal based sensor for characterization of mixtures and heterogeneous liquids, Sensors **22**, 2816 (2022).

[19] M. Sledzinska, B. Graczykowski, J. Maire, E. Chavez-Angel, C. M. Sotomayor-Torres, and F. Alzina, 2D phononic crystals: Progress and prospects in hypersound and thermal transport engineering, Adv. Funct. Mater. **30**, 1904434 (2020).

[20] M. Javadi, A. Heidari, and S. Darbari, Realization of enhanced sound-driven CNT-based triboelectric nanogenerator, utilizing sonic array configuration, Curr. Appl. Phys. **18**, 361 (2018).

[21] Z. Wen, W. Wang, A. Khelif, B. Djafari-Rouhani, and Y. Jin, A perspective on elastic metastructures for energy harvesting, Appl. Phys. Lett. **120**, 020501 (2022).

[22] A. Shakeri, S. Darbari, and M. Moravvej-Farshi, Designing a tunable acoustic resonator based on defect modes, stimulated by selectively biased PZT rods in a 2D phononic crystal, Ultrasonics **92**, 8 (2019).

[23] A. Khelif, Y. Achaoui, S. Benchabane, V. Laude, and B. Aoubiza, Locally resonant surface acoustic wave band gaps in a two-dimensional phononic crystal of pillars on a surface, Phys. Rev. B **81**, 214303 (2010).

[24] Y. Achaoui, A. Khelif, S. Benchabane, L. Robert, and V. Laude, Experimental observation of locally-resonant and Bragg band gaps for surface guided waves in a phononic crystal of pillars, Phys. Rev. B **83**, 104201 (2011).

[25] R. H. Parmenter, The Acousto-Electric Effect, Phys. Rev. **89**, 990 (1953).

[26] I. Constantinoiu and C. Viespe, ZnO metal oxide semiconductor in surface acoustic wave sensors: A review, Sensors **20**, 5118 (2020).

[27] X. Wang, L. Du, L. Cheng, S. Zhai, C. Zhang, W. Wang, Y. Liang, D. Yang, Q. Chen, and G. Lei, Pd/Ni nanowire film coated SAW hydrogen sensor with fast response, Sens. Actuators, B **351**, 130952 (2022).

[28] G. Y. Karapetyan, V. Kaydashev, D. Zhilin, M. Kutepov, T. Minasyan, and E. Kaidashev, A surface acoustic wave impedance-loaded high sensitivity sensor with wide dynamic range for ultraviolet light detection, Sens. Actuators, A **296**, 70 (2019).

[29] M. S. Brugger, L. G. Schnitzler, T. Nieberle, A. Wixforth, and C. Westerhausen, Shear-horizontal surface acoustic wave sensor for non-invasive monitoring of dynamic cell spreading and attachment in wound healing assays, Biosens. Bioelectron. **173**, 112807 (2021).

[30] Y. Guo, M. Schubert, and T. Dekorsy, Finite element analysis of surface modes in phononic crystal waveguides, J. Appl. Phys. **119**, 124302 (2016).

[31] A. Hutson and D. L. White, Elastic wave propagation in piezoelectric semiconductors, J. Appl. Phys. **33**, 40 (1962).

[32] I. A. Veres, T. Berer, O. Matsuda, and P. Burgholzer, Focusing and subwavelength imaging of surface acoustic waves in a solid-air phononic crystal, J. Appl. Phys. **112**, 053504 (2012).

[33] V. T. Rathod, A review of acoustic impedance matching techniques for piezoelectric sensors and transducers, Sensors **20**, 4051 (2020).

[34] B. H. Fisher and D. C. Malocha, Study of the acoustoelectric effect for SAW sensors, IEEE Trans. Ultrason. Ferroelectr. Freq. Control **57**, 698 (2010).